

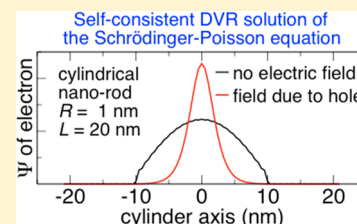
# An Infinite Order Discrete Variable Representation of an Effective Mass Hamiltonian: Application to Exciton Wave Functions in Quantum Confined Nanostructures

Alexey L. Kaledin,<sup>\*,†</sup> Tianquan Lian,<sup>‡</sup> Craig L. Hill,<sup>‡</sup> and Djamaladdin G. Musaev<sup>\*,†</sup>

<sup>†</sup>Cherry L. Emerson Center for Scientific Computation, Emory University, 1515 Dickey Dr., Atlanta, Georgia 30322, United States

<sup>‡</sup>Department of Chemistry, Emory University, 1515 Dickey Dr., Atlanta, Georgia 30322, United States

**ABSTRACT:** We describe an extension of the conventional Fourier grid discrete variable representation (DVR) to the bound state problem of a particle with a position-dependent mass. An infinite order DVR, derived for a variable mass kinetic energy operator, coupled with an efficient grid contraction scheme yields essentially exact eigenvalues for a chosen grid spacing. Implementation of the method is shown to be very practical due to the fact that in a DVR no integral evaluation is necessary and that the resultant kinetic energy matrix is sparse. Numerical calculations are presented for exciton states of spherical, cylindrical, and toric Type I (CdSe/ZnS) core-shell quantum dots. In these examples, electron-hole interaction is treated explicitly by solving a self-consistent Schrödinger-Poisson equation on a contracted DVR grid. Prospective applications of the developed approach to calculating electron transfer rates between adsorbed molecular acceptors and quantum confined nanocrystals of generic shape, dimensionality, and composition are also discussed.



## 1. INTRODUCTION

Quantization of energy is one of the most fundamental effects in quantum mechanics. Determination of bound states, i.e., eigenstates of a time-independent Schrödinger equation, is therefore of major importance in interpreting the spectra of atoms, molecules, molecular clusters, nanostructures, and other materials. The present paper is largely motivated by the latter, more specifically, by exploring novel theoretical treatments of the problem of electronic energy quantization in finite size semiconductor nanostructures or, commonly, quantum dots. Numerous studies of quantum dots have shown that the confinement effect on the bound state electron wave function and the corresponding energy can be well described by the so-called effective mass approximation (EMA) by treating an electron as a single particle with a nonconstant mass confined in a three-dimensional potential well.<sup>1–3</sup> There exist a variety of theoretical approaches for treating the generic bound state problem in the EMA, the most common of which include the usual basis set expansion of the wave function and standard grid-based discretization methods. Both of these families of approaches have been tested extensively on systems with EMA;<sup>4–7</sup> however, to the best of our knowledge, no studies of bound states of effective mass Hamiltonians have been reported using a discrete variable representation (DVR),<sup>8–11</sup> which is a member of the grid-based family of methods.

In this paper, we investigate the application of an infinite order DVR<sup>11</sup> on a Fourier grid to a single particle effective mass Hamiltonian. In other words, we expand the conventional approach, previously developed and applied to a variety of problems with constant mass, to the case of a coordinate dependent mass, which further generalizes DVR to the problem of quantum confined nanostructures. The usefulness of DVR is

further emphasized when one couples the Schrödinger equation with a generic Poisson equation, which is typically solved on a grid. We show that both equations can be solved simultaneously on the same (linear or nonlinear) DVR grid using exactly the same operator formalism.

Briefly, we wish to solve the one-particle Schrödinger equation with variable mass

$$\hat{H}\psi(\mathbf{r}) = E\psi(\mathbf{r}) \quad (1)$$

on a three-dimensional (3-D) Cartesian grid using an infinite order DVR, where  $\mathbf{r} \equiv (x, y, z)$ . For systems where the mass is position dependent, which is our focus, the proper Hamiltonian in eq 1 is<sup>12–14</sup>

$$\hat{H} = -\frac{\hbar^2}{2} \vec{\nabla}(\mathbf{r}) \cdot \left( \frac{1}{m^*(\mathbf{r})} \vec{\nabla}(\mathbf{r}) \right) + \tilde{V}(\mathbf{r}) \quad (2)$$

The effective potential  $\tilde{V}(\mathbf{r})$  in eq 2 is represented by the conduction band level of bulk material,<sup>1,2</sup> and may in addition contain electron-hole Coulombic interaction.<sup>7,15</sup> The form of the kinetic energy operator used in eq 2 imposes the well-known condition that the wave function is continuous everywhere, while its first derivative behaves as  $m_2 \partial \psi_1 / \partial R = m_1 \partial \psi_2 / \partial R$  at a mass-change boundary.<sup>12,13,16,17</sup> The subscripts 1 and 2 mark two adjacent regions of different mass, and  $R(\mathbf{r})$  is a coordinate crossing the 1–2 interface along its norm.

Received: April 2, 2014

Published: May 28, 2014

## 2. COMPUTATIONAL APPROACH

**2.1. DVR in 1-D.** First, we consider the one-dimensional (1-D) case. Using the completeness of the DVR basis, we write a generic expression for the kinetic energy operator as

$$\begin{aligned} \langle il | \frac{\partial}{\partial x} \frac{1}{m^*} \frac{\partial}{\partial x} | j \rangle &\equiv \sum_{k,k'} \langle il | \frac{\partial}{\partial x} | k \rangle \langle k | \frac{1}{m^*} | k' \rangle \langle k' | \frac{\partial}{\partial x} | j \rangle \\ &= \sum_k \frac{1}{m_k^*} \langle il | \frac{\partial}{\partial x} | k \rangle \langle k | \frac{\partial}{\partial x} | j \rangle \end{aligned} \quad (3)$$

invoking the property that a position operator, in this case the mass, is diagonal in DVR. From this equation it is clear that the  $\partial/\partial x$  operator must have a symmetric (or antisymmetric) representation so that the kinetic energy operator is ensured to be symmetric. The particle-in-a-box basis, typically used for a linear coordinate, can be shown to yield a nonsymmetric first derivative DVR matrix<sup>18</sup> and, consequently, a non-Hermitian kinetic DVR matrix. However, as shown before,<sup>11,19</sup> one can construct a symmetric DVR of the kinetic operator in the basis of eigenfunctions of  $\partial/\partial x$ , which are particle in a ring (plane wave) functions. Therefore, in the present paper, we take

$$\phi_n(x) = \frac{1}{\sqrt{b-a}} \exp \left[ i 2 \pi n \frac{x-a}{b-a} \right] \quad (4)$$

as the basis, where  $n = 0, \dots, \pm N$ , and  $(a, b)$  is the grid range with the  $2N + 1$  equally spaced points  $x_k = a + (b-a)k/(2N+1)$ ,  $k = 1, \dots, 2N+1$ . The grid spacing is thus  $\Delta x = (b-a)/(2N+1)$ . The point  $x = a$  is not on the grid due to the periodic boundary condition  $\phi_n(a) = \phi_n(b)$ .<sup>11</sup> The DVR matrix of the first derivative operator becomes

$$\begin{aligned} \langle kl | \frac{\partial}{\partial x} | j \rangle &= \frac{\Delta x}{b-a} \sum_{n=-N}^N \exp \left[ -i 2 \pi n \frac{x_k - a}{b-a} \right] \\ &\quad \left( \frac{\partial}{\partial x} \exp \left[ i 2 \pi n \frac{x - a}{b-a} \right] \right)_{x=x_j} \\ &= \frac{2\pi i}{2N+1} \frac{1}{b-a} \sum_{n=-N}^N n \exp \left[ i 2 \pi n \frac{j-k}{2N+1} \right] \end{aligned} \quad (5)$$

The sum in eq 5 can be calculated analytically, as shown by Tuvu and Band,<sup>19</sup> leading to

$$\langle kl | \frac{\partial}{\partial x} | j \rangle = -\frac{\pi}{b-a} \frac{(-1)^{k-j}}{\sin \left[ \pi \frac{k-j}{2N+1} \right]} \quad (6)$$

with the  $k = j$  element being zero. We note that the expression above is derived for an odd number of grid points and basis functions,  $2N + 1$ . Substituting eq 6 into eq 3 results in

$$\begin{aligned} \langle il | \frac{\partial}{\partial x} \frac{1}{m^*} \frac{\partial}{\partial x} | j \rangle &= (-1)^{i-j} \frac{\pi^2}{(b-a)^2} \\ &\quad \sum_{k \neq i,j}^{2N+1} \frac{1}{m_k^*} \frac{1}{\sin \left[ \pi \frac{i-k}{2N+1} \right] \sin \left[ \pi \frac{k-j}{2N+1} \right]} \end{aligned} \quad (7)$$

One can see that the first derivative DVR in plane-wave basis is anti-Hermitian, while the kinetic energy DVR is Hermitian, as they both should be. Equation 7 can be shown to reduce to the well-known closed form given elsewhere<sup>11,19</sup> if the mass is a constant (see below).

**2.2. DVR in 3-D.** To extend the 1-D DVR of the EMA kinetic operator to the 3-D case, we first write the 3-D Laplacian in eq 2 as a sum of its diagonal Cartesian components as  $(\partial/\partial x)(1/m_{xx}^*)(\partial/\partial x) + (\partial/\partial y)(1/m_{yy}^*)(\partial/\partial y) + (\partial/\partial z)(1/m_{zz}^*)(\partial/\partial z)$ , which is its common form if  $x, y, z$  are orthogonal. We note that in general the Laplacian may include the off-diagonal, i.e., mixed derivative, terms; however, in typical EMA applications, they are usually neglected.<sup>6,20</sup> In the present paper, the mass is a variable that is assumed to take on the corresponding bulk value in each layer of the semiconductor material, independent of the momentum direction, thus  $m_{xx}^* = m_{yy}^* = m_{zz}^* = m^*(x, y, z)$ . Because the DVR basis function in 3-D is a direct product of the three components, one for each Cartesian dimension, we write it by extending the matrix element in eq 7 to 3-D while treating the mass as a function of  $x, y, z$ ,

$$\begin{aligned} \langle ijkl | \vec{\nabla}(\mathbf{r}) \cdot \left( \frac{1}{m^*(\mathbf{r})} \vec{\nabla}(\mathbf{r}) \right) | i'j'k' \rangle &= \delta_{ij} \delta_{kk'} \sum_{a \neq i,i'}^{2N+1} \frac{1}{m^*(x_a, y_j, z_k)} \nabla_{ia} \nabla_{ai'} \\ &\quad + \delta_{ii} \delta_{kk'} \sum_{\beta \neq j,j'}^{2N+1} \frac{1}{m^*(x_i, y_\beta, z_k)} \nabla_{j\beta} \nabla_{\beta j'} \\ &\quad + \delta_{ii} \delta_{jj'} \sum_{\gamma \neq k,k'}^{2N+1} \frac{1}{m^*(x_i, y_j, z_\gamma)} \nabla_{k\gamma} \nabla_{\gamma k'} \end{aligned} \quad (8)$$

where the elements  $\nabla_{rs}$  are defined in eq 6. Unlike in the constant mass DVR case, the individual Cartesian kinetic energy components depend on four indices due to mass's dependence on the three Cartesian coordinates. Adding the kinetic operator in its DVR matrix representation to Hamiltonian in eq 2 leads to the Hamiltonian matrix

$$\begin{aligned} \langle ijkl | \hat{H} | i'j'k' \rangle &= -\frac{\hbar^2}{2} \langle ijkl | \vec{\nabla}(\mathbf{r}) \cdot \left( \frac{1}{m^*(\mathbf{r})} \vec{\nabla}(\mathbf{r}) \right) | i'j'k' \rangle \\ &\quad + \delta_{ii} \delta_{jj} \delta_{kk'} \tilde{V}(x_i, x_j, x_k) \end{aligned} \quad (9)$$

Because the matrix is structured, in practical implementation only the three kinetic matrix blocks (eq 7) and the diagonal potential need to be stored in memory.

**2.3. DVR Representation of the Poisson Equation and Self-Consistent Electron-Hole Wave Functions.** The potential operator appearing in eqs 2 and 9 may contain additional terms due to electron-hole electrostatic interactions. For the simple case where the dielectric medium is uniform, the interaction is the usual two-center Coulomb integral over all space. However, for nonuniform dielectric media, one has to solve the self-consistent Schrödinger-Poisson equation<sup>21</sup> to properly account for charge polarization across all interfaces. In atomic units, consistent with eq 2, the Poisson equation for the electron(hole) potential due to the electron(hole) density is<sup>22,23</sup>

$$\vec{\nabla} \cdot \epsilon_r(\mathbf{r}) \vec{\nabla} \Phi(\mathbf{r}) = -4\pi \rho(\mathbf{r}) \quad (10)$$

where  $\epsilon_r(\mathbf{r}) \equiv \epsilon(\mathbf{r})/\epsilon_0$  is the coordinate-dependent relative (to vacuum) permittivity of the medium, and  $\rho(\mathbf{r}) = q\psi(\mathbf{r})/l^2$  ( $q = -1$  for the electron and  $q = 1$  for the hole). Common solutions of Poisson's equation involve numerical discretization by low order finite differences, although it is obvious that the same DVR formalism used for the Schrödinger equation can be applied to eq 10. Inserting the identity and projecting both sides onto grid point  $\langle ijkl$  results in the matrix equation

$$\sum_{i'j'k'} \langle ijkl | \vec{\nabla} \cdot \epsilon_r(\mathbf{r}) \vec{\nabla} | i'j'k' \rangle \langle i'j'k' | \Phi(\mathbf{r}) \rangle = -4\pi \langle ijkl | \rho(\mathbf{r}) \rangle \quad (11a)$$

or equivalently

$$\sum_{i'j'k'} F_{ijk,i'j'k'} \Phi_{i'j'k'} = -4\pi \rho_{ijk} \quad (11b)$$

where the elements  $F_{ijk,i'j'k'}$  are calculated using eqs 7 and 8, and the potential and the density are defined on the same grid. Equation 11 is solved using the linear conjugate gradient method.

To incorporate electron–hole interaction into eq 2, we add the density-dependent electrostatic potential  $\Phi$  to the confinement potential and solve the corresponding eigenvalue equations for electron and hole simultaneously until both densities become stationary. Namely,

$$(\hat{H}_e - \Phi_h[\rho_h(\mathbf{r})])\psi_e^{\text{SCF}}(\mathbf{r}) = E_e^{\text{SCF}}\psi_e^{\text{SCF}}(\mathbf{r}) \quad (12a)$$

for the electron and

$$(\hat{H}_h + \Phi_e[\rho_e(\mathbf{r})])\psi_h^{\text{SCF}}(\mathbf{r}) = E_h^{\text{SCF}}\psi_h^{\text{SCF}}(\mathbf{r}) \quad (12b)$$

for the hole. The electron–hole interaction energy is then evaluated using either potential,

$$\langle v_{e-h} \rangle = \int d\mathbf{r} \rho_e(\mathbf{r}) \Phi_h(\mathbf{r}) = \int d\mathbf{r} \rho_h(\mathbf{r}) \Phi_e(\mathbf{r}) \quad (13)$$

Extension of the Schrödinger–Poisson DVR scheme to multiexciton systems is straightforward provided that proper wave function symmetrization due to half-integer spin particles is made. This is routinely done in electronic structure calculations and can be readily incorporated into eq 12.

**2.4. Grid Contraction.** As mentioned above, the use of the plane-wave basis introduces artificial interactions with periodic image cells. It is possible to virtually eliminate image interaction by isolating the original cell, i.e., taking  $b - a \rightarrow \infty$ , which also implies that  $N \rightarrow \infty$ . This was first proposed by Light and co-workers for finite grids<sup>8</sup> and later advocated by Colbert and Miller for infinite grids.<sup>11</sup> In practice, this can be achieved by evaluating the sums in eq 8 for progressively larger values of  $N$  until convergence while keeping only a subset of matrix elements (grid points)  $\langle ijkl | H | i'j'k' \rangle$ . In other words, an arbitrarily large grid chosen initially to minimize image cell interaction is contracted to a much smaller subset of  $ijk$  points surrounding the original cell. The contraction is done according to the shape of the potential and to the rate of decay of the wave function at the outer edges. The latter condition requires that some cutoff criteria be imposed. For calculations of particle wave functions, in finite confinement potentials, we cannot use an energy cutoff but instead set a distance cutoff criterion. For a spherical structure, we determine the smallest value for a cutoff radius  $R_c$  by doing a few calculations until the norm of the wave function at the grid's boundary  $|\psi((x_i^2 + y_i^2 + z_i^2)^{1/2} = R_c)|$  becomes acceptably small, e.g.,  $<10^{-5}$ . Similar criteria can be chosen for arbitrary shapes.

It is important to show that the sums in eqs 7 and 8 converge as  $N \rightarrow \infty$ . (For the particle-in-a-box DVR basis and the special case of constant mass, this was shown analytically by Colbert and Miller.<sup>11</sup>) To demonstrate convergence, we substitute  $m_i^* = m$  in eq 7 and calculate the right-hand side of these equations. Here, we recast the result of Tuvi and Band<sup>19</sup> for the kinetic

energy operator in 1-D using the grid parameters defined for eq 4

$$T_{ii} = \frac{\hbar^2}{2m} \left( \frac{2\pi}{b-a} \right)^2 \frac{N(N+1)}{3} \quad (14a)$$

and

$$T_{ij} = (-1)^{i-j} \frac{\hbar^2}{2m} \left( \frac{2\pi}{b-a} \right)^2 \frac{\cos\left(\pi \frac{i-j}{2N+1}\right)}{2\sin^2\left(\pi \frac{i-j}{2N+1}\right)} \quad (14b)$$

Taking the limit  $N \rightarrow \infty$  and using  $(b-a) = \Delta x(2N+1)$  leads to the well-known result<sup>11</sup>

$$T_{ii}^\infty = \frac{\hbar^2 \pi^2}{6m \Delta x^2} \quad (15a)$$

and

$$T_{ij}^\infty = \frac{(-1)^{i-j} \hbar^2}{m \Delta x^2 (i-j)^2} \quad (15b)$$

In other words, grid contraction for plane-wave DVR basis accomplishes two important goals: (i) The artificial interaction with image cells is removed. (ii) The Hamiltonian matrix and therefore the wave function are essentially exact, i.e., converged for a given grid spacing  $\Delta x$  and wave function cutoff radius  $R_c$ . Both of these parameters can be tuned to yield wave functions and energies as close to the exact limit as desired.

We briefly note that for a variable mass eqs 14 and 15 cannot be written in a closed form, and we have to carry out the summation numerically, which in practice constitutes a negligible fraction of the entire computational effort. The main effort is matrix diagonalization, which is carried out using an iterative procedure. We define a small subspace, typically 10–20 vectors, and apply Davidson's procedure<sup>24</sup> for the lowest root until the norm of the residual is less than  $10^{-5}$ . Higher roots, if necessary, are obtained in the same fashion after projecting out the already converged roots.

**2.5. Recovering the Wave Function and Electrostatic Potential Using the Infinite Grid.** Numerical solutions of Schrödinger and Poisson's equations yield the values of the wave function and electrostatic potential, respectively, only at the grid points. However, it is possible to recover both analytically in terms of the sinc function, i.e.,  $\sin(x)/x$ , anywhere in the coordinate space provided that the infinite grid limit has been taken, as suggested by Colbert and Miller.<sup>11</sup> A generic DVR solution  $\psi$  (we may substitute  $\Phi$  for Poisson's equation solution) can be written in terms of the discrete basis states (position states)

$$\langle x | \psi(x) \rangle = \sum_i \langle x | x_i \rangle \psi_i \quad (16)$$

where  $\psi_i$  is the value of the wave function at the grid point  $i$ . Clearly, for the special case of  $x = x_j$  (a grid point),  $\psi(x_j) = \psi_j$ . For all other cases, we calculate the overlap explicitly by substituting eq 4 into eq 17

$$\langle x | x_i \rangle = \Delta x \sum_n \phi_n(x) \phi_n(x_i) \quad (17)$$

After some manipulation, we obtain

$$\begin{aligned}\langle x|x_i\rangle &= \frac{\Delta x}{b-a} \left( 1 + 2 \sum_{n=1}^N \cos \left[ 2\pi n \frac{x-x_i}{b-a} \right] \right) \\ &= \frac{\Delta x}{b-a} \frac{\sin \left[ 2\pi(N+1/2) \frac{x-x_i}{b-a} \right]}{\sin \left[ \pi \frac{x-x_i}{b-a} \right]}\end{aligned}\quad (18)$$

where we have used convergence of a geometric series to arrive at the closed form expression. For the infinite order DVR where  $N \rightarrow \infty$  and  $b-a \rightarrow \infty$  while  $\Delta x = (b-a)/(2N+1)$  is finite, eq 18 has the limit

$$\lim_{\substack{N \rightarrow \infty \\ b-a \rightarrow \infty}} \langle x|x_i\rangle = \frac{\sin \left[ \pi \frac{x-x_i}{\Delta x} \right]}{\pi \frac{x-x_i}{\Delta x}} = \text{sinc} \left[ \pi \frac{x-x_i}{\Delta x} \right] \quad (19)$$

Substituting eq 19 into eq 16 and extending to the 3-D case, we have

$$\begin{aligned}\psi(x, y, z) &= \sum_{i,j,k} \psi_{ijk} \text{sinc} \left( \pi \frac{x-x_i}{\Delta x} \right) \text{sinc} \left( \pi \frac{y-y_j}{\Delta y} \right) \\ &\quad \text{sinc} \left( \pi \frac{z-z_k}{\Delta z} \right)\end{aligned}\quad (20)$$

where  $\psi_{ijk}$  is the value of the eigenfunction at the grid point  $(x_i, y_j, z_k)$ . Utility of eq 20 becomes obvious when calculating electron wave function overlaps between neighboring structures, e.g., between a quantum dot and an adsorbed molecule.

### 3. RESULTS

**3.1. Grid Tuning in 1-D.** It is important to investigate convergence of the Hamiltonian matrix (eq 9) with respect to  $N$ . Once again, we take a 1-D case. The used grid end points are  $a = -(N+1)\Delta x$  and  $b = N\Delta x$ , and grid spacing is  $\Delta x = 2$  bohr. The applied potential and mass parameters correspond to a Type I CdSe/ZnS core-shell quantum dot with core radius of  $R_0 = 25.89$  bohr and uniform ZnS shell thickness of  $D = 15$  bohr are taken from the experiment.<sup>25</sup> Figure 1 provides a detailed overview of the test system.

The applied grid contraction scheme is such that only the gridpoints on the  $(-50,50)$  bohr segment are used for constructing the Hamiltonian matrix, which is equivalent to forcing the wave function to vanish for all  $|x| > 50$  bohr. For analysis, we choose three representative matrix elements: (1) a diagonal element  $H_{1,1}$ , (2) large off-diagonal element  $H_{1,2}$ , and (3) small off-diagonal element  $H_{1,25}$ . All three elements show very similar convergence rates as  $N \rightarrow \infty$  and are practically at their limit for  $2N+1 > 801$ . For instance, the difference in  $H_{ij}$  between  $2N+1 = 4001$  and  $2N+1 = 8001$  (not shown in Figure 2) is  $\sim 0.1$  meV ( $\sim 1$  cm<sup>-1</sup>). We suggest that a numerically acceptable value for  $2N_{\text{max}}+1$  can be chosen at 501, and  $a = -502$  bohr and  $b = 500$  bohr. With these definitions, the interaction with image cells is completely eliminated.

Next, we determine the largest value of grid spacing  $\Delta x$  with which converged eigenvalues are achieved. Figure 3 shows the behavior of the three lowest eigenvalues with decreasing  $\Delta x$ ; for comparison, we also plot the results of first order finite difference, FD, which should represent the upper bound in the relative error. Analyzing the DVR calculation, the ground state eigenvalue is nearly flat with  $\Delta x$ , deviating from the converged limit by less than 5 meV. The excited states are more sensitive,

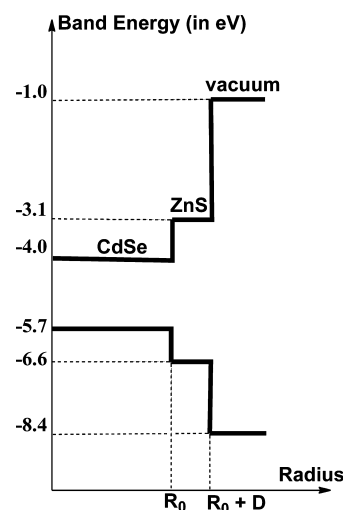


**Figure 1.** Energy level diagram of the Type I (CdSe/ZnS) QD with a CdSe core of radius  $R_0$  and a ZnS shell of thickness  $D$ . The horizontal lines mark the levels of band energies of the CdSe core, ZnS shell, and vacuum. The conduction and valence band levels of vacuum correspond to those of the surrounding solvent. The vertical lines mark the positions of the two interfaces: core-shell and shell-vacuum. The respective effective masses are 0.13, 0.25, 1.0  $m_e$  for the electron and 0.45, 1.3, 1.0  $m_e$  for the hole, and the respective dielectric constants are 10, 8.9, and 1  $\epsilon_0$  for the core, shell, and vacuum. These parameters are taken from ref 25.

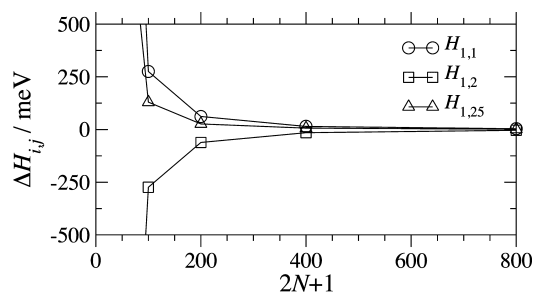


**Figure 2.** Convergence of the Hamiltonian matrix with respect to grid size. The full matrix is  $51 \times 51$  of which three representative elements are depicted. The Hamiltonian corresponds to that of a 1-D CdSe/ZnS quantum dot with  $V = -3$  eV and  $m^* = 0.13 m_e$  for  $|x| < 25.89$  bohr,  $V = -2.7$  eV and  $m^* = 0.25 m_e$  for  $25.89 < |x| < 40.89$  bohr, and  $V = 0$  and  $m^* = 1 m_e$  otherwise. These parameters are taken from ref 25. The grid spacing is  $\Delta x = 2$  bohr.

converging at  $\Delta x = 1$  bohr. For all three states, however, the error with respect to the eigenvalue at  $\Delta x = 0.25$  bohr is less than 1% regardless of  $\Delta x$ . Relative to DVR, the FD ground state converges noticeably slower, with the equivalent DVR limit ( $\Delta x = 4.0$  bohr) achieved around  $\Delta x = 0.5$  bohr. Similar behavior is observed for the two excited states. We recall that the de Broglie wavelength  $\lambda$  of an electron in vacuum with kinetic energy of 1 eV, the order of confinement energies considered here, is  $\sim 23$  bohr. The behavior of the DVR eigenstates with  $\Delta x$  is consistent with the prescription<sup>11</sup> of 4–5 points per  $\lambda$  implying that even a coarse grid,  $\Delta x = 4$  bohr, is easily sufficient for obtaining reliable ground states energies of the system shown in Figure 3. Nevertheless, in the calculations of 3-D quantum dots presented below, we use  $\Delta x = 2$  bohr grid spacing for two main reasons: (i) to better converge the lower lying excited states and (ii) to properly sample thin ZnS shells (the thinnest shell is only 5 bohr).



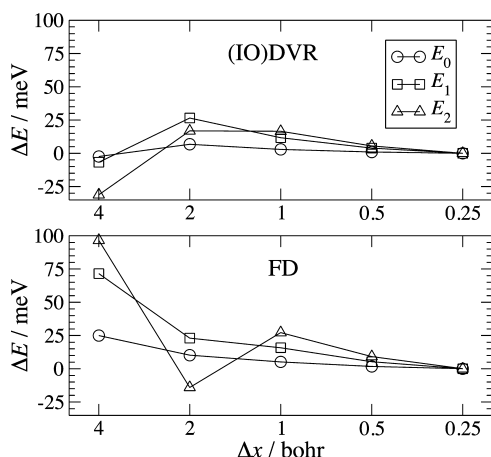


**Figure 3.** Convergence of the ground and the first and second excited states of a 1-D model Type I CdSe/ZnS quantum dot with respect to grid spacing  $\Delta x$  (plotted on a log scale) for the infinite order (IO)DVR and the first order finite difference FD methods. Five values of  $\Delta x$ , with the corresponding  $N$ , are considered for fixed  $a = -(8000 + \Delta x)$  and  $b = 8000$  bohr. The grid is contracted onto a  $(-50, 50)$  bohr segment resulting in reduced number of grid points: 26, 51, 101, 201, and 401, respectively.

**3.2. DVR Calculations of CdSe/ZnS Type I Spherical QDs.** Upon tuning the parameters (grid points  $N$ , grid dimension  $b - a$ , and grid spacing  $\Delta x$ ), we apply an infinite order DVR to calculation of electron and hole states in Type I CdSe/ZnS core-shell QDs. We use a radius  $R_0 = 25.89$  bohr ( $13.7 \text{ \AA}$ ) and three ZnS shell layers of  $\Delta D = 5$  bohr ( $2.646 \text{ \AA}$ ) each, which corresponds roughly to a single layer of ZnS. The grid is defined as discussed in section 3.1. The uncontracted grid is constructed using  $\Delta x = \Delta y = \Delta z = 2$  bohr,  $a_x = a_y = a_z = -802$  and  $b_x = b_y = b_z = 800$  bohr, with a total set of  $801^3$  (more than half of billion) points. The Hamiltonian matrix is then calculated and stored on a subset of  $M$  points satisfying the  $(x_i^2 + y_j^2 + z_k^2)^{1/2} < 50$  bohr condition. Thus, the contracted grid consists of  $M = 65117$  points, which is the size of the matrix to be diagonalized. The DVR matrix was constructed with the electron (hole) effective masses being equal to 0.13 ( $0.45 m_e$ ) for CdSe and 0.25 ( $1.3 m_e$ ) for ZnS. The masses in the vacuum or organic ligand, i.e., the region outside the outer shell of the QD, are set to  $1 m_e$ . We note that calculations for a similar system, albeit with different bulk parameters, have been reported by others.<sup>7</sup> In the present paper, the bulk parameters described above are taken from the more recent experiments<sup>25</sup> (Figure 1).

Calculations of 1S ground state energies are presented in Table 1. The electron confinement energy is virtually insensitive to the thickness of ZnS shell, while that of the hole has a significant shift down, 0.079 eV or 26%, from  $D = 0$

to  $D = 5$  bohr ZnS shell. For comparison, we also provide the previously reported band gap values calculated using the matching boundary value approach.<sup>25</sup> The shown band gaps are corrected by electron-hole Coulomb interaction, which is calculated using eq 13 with the corresponding CdSe/ZnS dielectric constants (Figure 1). The two calculations agree very well and follow the same trend.

The differences between the electron and hole ground state wave functions (Figure 4) carry important implications for electron transfer dynamics. Due to electron's significantly smaller mass in the core ( $0.13$  vs  $0.45 m_e$ ), it extends appreciably farther outside the core than does the hole, despite the higher confinement barrier ( $3.0$  vs  $2.7$  eV). This behavior was noted previously and used in designing a charge separation experiment by coating the CdSe core with a layer of ZnS of varying thickness.<sup>25</sup> The hole has a bigger effective mass in ZnS than in CdSe, and its density decays at a faster rate in the shell medium. This essentially prevents the electron that has transferred to an adsorbed electron acceptor, from recombining with the hole. Assuming the charge separation/recombination rate is proportional to the electron-hole density at the interface, a simple exponential dependence of the rate on shell thickness has been proposed, namely,  $k_{ET} \propto \exp(-\beta D)$ .<sup>25</sup> Fitting the exponential to the four values of the density obtained from the calculations for  $D = 0, 5, 10, 15$  bohr gives the respective separation/recombination exponents 0.39 and 1.01 per  $\text{\AA}$ , qualitatively consistent with the 0.35 and  $0.91 \text{ \AA}^{-1}$  values derived from the experimental data.<sup>25</sup>

Excited states are expected to play an important role in determining photophysical properties of quantum dots. In particular, electron transfer to acceptors can be impacted by low-lying excited states mixing with the ground state in nonspherical structures. Table 2 and Figure 4 provide overviews of low-lying excited states of electron and hole. For illustrative comparison, we also plot 2-D projections of the electron and hole orbitals, represented by eq 16, for the largest quantum dot ( $D = 15$  bohr). The 1S orbitals are isotropic and nodeless with a discernible step-like structure at the core-shell interface ( $x, y = \pm 25.89$  bohr). Nodal  $xz$  and  $yz$  planes passing through the origin are clearly visible in 1P and 1D orbitals. We note that for degenerate orbitals,  $xyz$  spatial mixing is arbitrary. The 2S orbitals have the nodal surface at  $R \approx 23.5$  bohr for the electron and  $R \approx 17.6$  bohr for the hole. As expected, the hole orbitals are much more compact than the corresponding ones for the electron.

**3.3. Electrostatic Confinement in Nanorods.** Despite the relative strength of electron-hole attraction in the spherical examples shown above, the Coulomb correction to the one-particle wave functions is known to be marginal, while the properties of confined excitons are well described by the first order perturbation theory.<sup>7,26</sup> On the other hand, if one of the

**Table 1.** Electron and Hole 1S State DVR Confinement Energies ( $\Delta E_e$ ,  $\Delta E_h$ ), Coulombic Electron-Hole Stabilization Energy  $\langle v_{e-h} \rangle$ , and Band Gap ( $BG_0 = 1.7$  eV, Figure 1) for the Bare CdSe Core ( $D = 0$ ) and Three Cases of ZnS Shell Thickness  $D$  (bohr)<sup>a</sup>

$D$	$\Delta E_e$	$\Delta E_h$	$\langle v_{e-h} \rangle$	$BG^b$	$BG^c$
0	0.56711	0.30724	-0.15133	2.42302	2.4189
5	0.56108	0.22825	-0.13404	2.35529	2.3337
10	0.55805	0.22271	-0.12963	2.35113	2.3208
15	0.55576	0.22228	-0.12777	2.35027	2.3162

<sup>a</sup>All energies are in eV. <sup>b</sup>Band gap is defined as  $BG = BG_0 + \Delta E_e + \Delta E_h + \langle v_{e-h} \rangle$ . <sup>c</sup>Taken from ref 25.

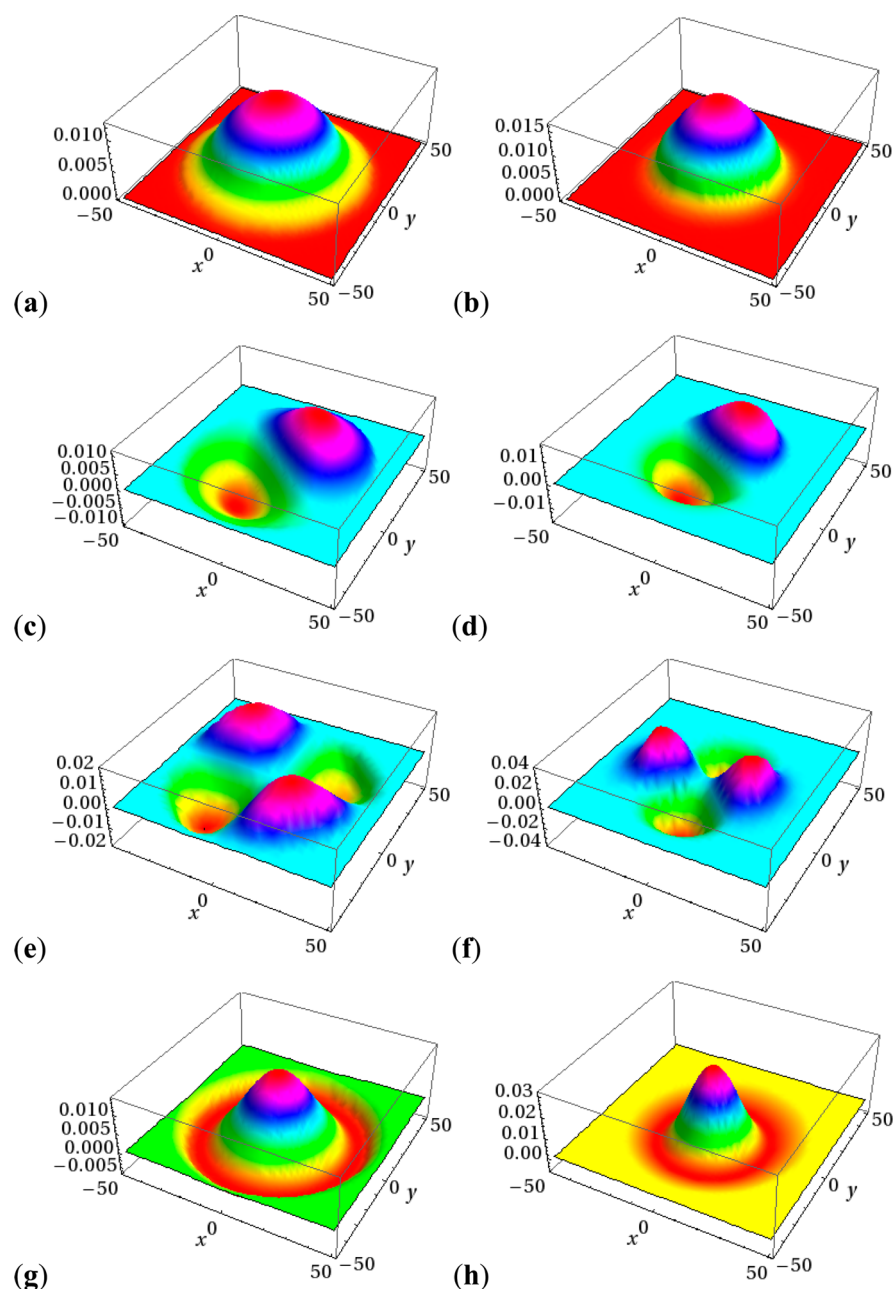


**Figure 4.** Exemplary 2-D drawings of electron and hole DVR orbitals of a spherical Type I quantum dot with a 25.89 bohr CdSe core radius and a 15 bohr Å ZnS shell shown as  $xy$ -plane projections for electron–hole 1S (a,b), 1P (c,d), 1D (e,f), and 2S (g,h).

**Table 2. Electron and Hole Excited Bound States of the Type I CdSe/ZnS Core–Shell Quantum Dots with Various Shell Thickness  $D$  (bohr)<sup>a</sup>**

$E_{\Gamma} - E_{1S}$	$D = 0$	$D = 5$	$D = 10$	$D = 15$
$\Gamma = 1P_e$	0.76666	0.64290	0.58138	0.54314
$\Gamma = 1D_e$	1.74283	1.39448	1.18033	1.03229
$\Gamma = 2S_e$	2.55058	2.05668	1.57285	1.21467
$\Gamma = 1P_h$	0.32424	0.25555	0.24739	0.24617
$\Gamma = 1D_h$	0.72881	0.57547	0.54832	0.54180
$\Gamma = 2S_h$	0.94764	0.80400	0.76063	0.73903

<sup>a</sup>Subscript e/h is used to distinguish electron–hole orbitals. The energies in eV are relative to 1S.

three spatial dimensions is significantly greater than the other two, such as in quantum nanorods, one has to include electrostatic confinement simultaneously with the spatial confinement by solving the self-consistent Schrödinger–

Poisson equation. In this section, we demonstrate robustness of DVR in such applications by considering a 20 nm long cylindrical CdSe nanorod of radius 1 nm submerged in a medium of varying permittivity. Placing the center at the origin

and aligning the cylinder's axis along  $z$ , we lay down the following uniform Cartesian grid:  $[-802, 800]$  bohr for  $x$  and  $y$  and  $[-918, 900]$  bohr for  $z$  with  $\Delta x = \Delta y = 2$  bohr and  $\Delta z = 18$  bohr. We then contract the grid to  $[-28, 28]$  bohr and  $[-396, 396]$  bohr for  $(x, y)$  and  $z$ , respectively, by requiring that the wave function vanishes at all points beyond  $|z_{\text{cut}}| = 400$  bohr and  $(x_{\text{cut}}^2 + y_{\text{cut}}^2)^{1/2} = 30$  bohr and construct Hamiltonian and Poisson matrices. The size of the matrices is 31,365 (down from 64,801,701 of the uncontracted rectangular grid).

In these calculations, we observe the ratio of Schrödinger-to-Poisson equation iterations (i.e., Davidson-to-conjugate gradient) to be about 10 in the early SCF cycles and about 1 in the late SCF cycles. This suggests that the method scales essentially as matrix diagonalization and can be easily improved by applying an exact conjugate gradient-based preconditioner to the Davidson cycle.

The effect of Coulomb interaction on the wave function is clearly shown in Figure 5 where we compare a field-free

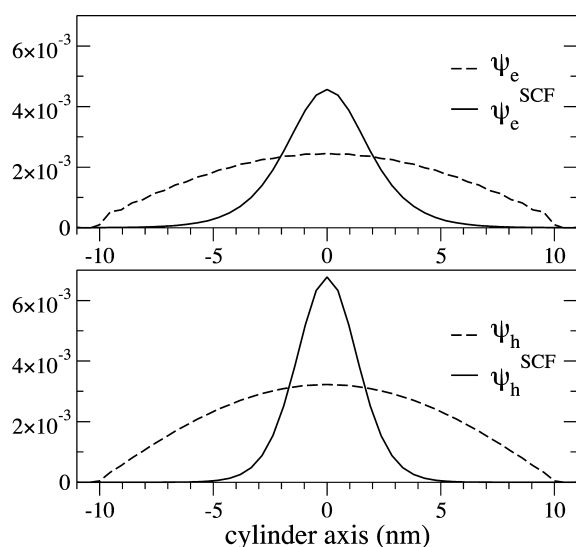


**Figure 5.** Plot of the ground state electron (upper graph) and hole (lower graph) wave functions with Coulomb interaction (solid line) and without (dashed line) for a 20 nm long CdSe cylinder of radius 1 nm placed in vacuum.

calculation with a self-consistent solution of the Schrödinger–Poisson equation (eq 12). In the noninteracting particle case, both wave functions stretch along the length of the nanorod behaving like particle-in-a-box states, i.e.,  $\langle z|\psi\rangle \sim \cos(\pi z/L)$  for  $L = 20$  nm. When the electron–hole interaction is turned on, the wavefunctions contract along the  $z$ -axis reflecting the effect of strong Coulombic confinement.

In a more detailed analysis, summarized in Table 3, we compare electron–hole spatial separation for four cases: “field

free” calculation, strong solvent, weak solvent, and vacuum. When fully uncoupled, the electron and hole are separated, on average, by nearly 4.8 nm (4.6 along  $z$ ), a distance more than twice greater than the diameter of the nanorod. With the interaction included, the electron–hole spatial proximity is amplified by the decreasing medium permittivity leading to increasingly stronger interface polarization, which acts so as to contract the wave functions along the  $z$ -axis (Figure 5). Thus, a “strong solvent” environment barely confines the exciton along the nanorod’s longitudinal axis, while a “weak solvent” and especially the vacuum create a closely confined electron–hole pair. Notably, the lateral separation is virtually insensitive to the medium

**3.4. Efficiency of Grid Contraction Scheme.** A further demonstration of the efficiency of a 3-D DVR grid contraction scheme can be carried out using a torus model. We consider a torus with a major radius  $\rho_0$  and a minor radius  $r_0$ . Using the same definitions for the full (uncontracted) grid and material parameters as in the calculations for the spherical QDs above, while grounding the wave function at the grid points that fall outside a cutoff radius  $r_{\text{cut}} > r_0$ , we solve the secular equations for electron and hole. Calculations show that converged eigenvalues for a test system  $\rho_0 = 25.89$  and  $r_0 = 5$  bohr are achieved with  $r_{\text{cut}} = 15$  bohr. Using these  $r_0$  and  $r_{\text{cut}}$ , we consider four torii with  $\rho_0, 2\rho_0, 3\rho_0$ , and  $4\rho_0$ . Because the volume of a torus grows linearly with the major radius, the number of retained (intrinsic) grid points  $M$  also grows exactly linearly, despite the fact that the volume of the box enclosing the torus and the corresponding number of associated rectangular Cartesian grid points  $M'$  grow quadratically, as shown in Table 4. In other words, any standard finite grid (or

**Table 4.** Rectangular Grid Size  $M'$  (non-intrinsic grid), DVR Matrix Size  $M$  (intrinsic grid), and Confinement Energies in eV of Electron and Hole of Four Toric CdSe QDs with Major Radius  $n\rho_0$  with ( $\rho_0 = 25.89$  bohr), Minor Radius 5 bohr, and Minor Cutoff Radius 15 bohr<sup>a</sup>

$n$	$M'$	$M$	$\Delta E_e$	$\Delta E_h$
1	25 215	14 448	1.923	1.619
2	67 335	28 892	1.924	1.620
3	129 735	43 340	1.917	1.611
4	212 415	57 762	1.929	1.623

<sup>a</sup>Material parameters are those shown in Figure 1.

uncontracted grid) method, such as finite differences, would not take advantage of the intrinsic potential shape and would formally scale as  $M'$  (Table 4).

The same linear or quasi-linear scaling of intrinsic grid points and consequently of the matrix size can be demonstrated for  $n$ -fold torii and torii of arbitrary shape. The implication of linear scaling of DVR grid size for a generic torus is particularly

**Table 3.** Variation of Electron–Hole Spatial Separation (nm), Confinement, and Coulombic Attraction Energies (meV) in a 20 nm Long Cylindrical Nanorod of Radius 1 nm with the Relative Permittivity ( $\epsilon_r$ ) of the Surrounding Medium<sup>a</sup>

	$\langle  r_e - r_h  \rangle$	$\Delta_z$	$\Delta_{xy}$	$\Delta E_e$	$\Delta E_h$	$\langle v_{e-h} \rangle$
field-free environment	4.791	4.617	0.819	514.9	299.7	0
$\epsilon_r = 100$ (strong solvent)	4.023	3.824	0.818	505.9	290.7	−9.5
$\epsilon_r = 10$ (weak solvent)	3.100	2.854	0.817	492.2	276.3	−26.2
$\epsilon_r = 1$ (vacuum)	1.671	1.285	0.819	320.4	91.7	−228.2

<sup>a</sup> $\epsilon_r$  of CdSe is 10. The cylinder’s axis is along  $z$ .

important for efficient grid sampling of lower dimensional QDs, such as nanowires and nanodisks.

#### 4. CONCLUDING REMARKS

We have shown how the conventional Fourier grid discrete variable representation can be used to treat the bound state problem of a particle with a position-dependent mass. An infinite order representation, derived specifically to treat the case of a variable mass, coupled with an efficient grid contraction scheme yields converged electron and hole energy levels for a chosen grid spacing,  $\Delta x$ . The derived matrix elements have a simple and easily implementable form. The main computational effort is found to be in the diagonalization of the resultant matrix, which due to its sparseness can be done very efficiently using iterative methods. We also demonstrate that the same DVR procedure can be used to electrostatically couple an electron with a hole by solving the generic Poisson equation in tandem with the Schrödinger equation. To our knowledge, this derivation of an infinite order DVR for a Schrödinger–Poisson equation is novel and is one of the main features of the present work.

Because the DVR described here can be defined on any set of points (provided they are a subset of a larger uniform grid), it is ideally suited for calculations of quantum dots of generic shape and composition as well as quantum dots of lower dimensionality, such as nanorods, nanowires, nanodisks, etc. The DVR approach can also be extended to more sophisticated treatments of QD and material band structure, including multiexciton coupled electron–hole systems and multiband effective mass approximation theories.

Furthermore, we show that the obtained eigenfunctions have a simple analytical representation which is valid anywhere in the coordinate space. This opens the possibility to calculate spatial overlaps of electron–hole orbitals of quantum dots with molecular orbitals of adsorbed ligands, chromophores, and/or catalysts for the purpose of estimating quantum mechanical electron transfer amplitudes. Any integrals involving eq 16 can be calculated as a function of a QD–molecule reaction coordinate either numerically by merging grids or analytically by utilizing molecular basis functions as LCAOs. Applications of Marcus's electron transfer theory and real-time wavepacket propagation using eigenstates are obvious extensions of this method.

#### AUTHOR INFORMATION

##### Corresponding Authors

\*E-mail: akaledi@emory.edu.

\*E-mail: dmusaev@emory.edu.

##### Notes

The authors declare no competing financial interest.

#### ACKNOWLEDGMENTS

The authors acknowledge the U.S. Department of Energy, Office of Basic Energy Sciences, Solar Photochemistry Program (DE-FG02-07ER-15906) for support. We also gratefully acknowledge NSF MRI-R2 Grant CHE-0958205 and the use of the resources of the Cherry Emerson Center for Scientific Computation.

#### REFERENCES

- (1) Brus, L. E. *J. Chem. Phys.* **1983**, *79*, 5566–5571.
- (2) Brus, L. E. *J. Chem. Phys.* **1984**, *80*, 4403–4409.
- (3) Efros, A. L.; Rosen, M. *Phys. Rev. B* **1998**, *58*, 7120–7135.
- (4) Fonseca, L. R. C.; Jimenez, J. L.; Leburton, J. P.; Martin, R. M. *Phys. Rev. B* **1998**, *57*, 4017–4026.
- (5) Roy, M.; Maksym, P. A. *Phys. Rev. B* **2003**, *68*, 235308:1–7.
- (6) Maia, A. D. B.; da Silva, E. C. F.; Quivy, A. A.; Bindilatti, V.; de Aquino, V. M.; Dias, I. F. L. *J. Appl. Phys.* **2013**, *114*, 083708:1–9.
- (7) Sahin, M.; Nizamoglu, S.; Kavruk, A. E.; Demir, H. V. *J. Appl. Phys.* **2009**, *106*, 043704:1–5.
- (8) Light, J. C.; Hamilton, I. P.; Lill, J. V. *J. Chem. Phys.* **1985**, *82*, 1400–1409.
- (9) Bacic, Z.; Light, J. C. *J. Chem. Phys.* **1986**, *85*, 4594–4604.
- (10) Kosloff, R. *J. Phys. Chem.* **1988**, *92*, 2087–2100.
- (11) Colbert, D. T.; Miller, W. H. *J. Chem. Phys.* **1992**, *96*, 1982–1991.
- (12) Harrison, W. A. *Phys. Rev.* **1961**, *123*, 85–89.
- (13) BenDaniel, D. J.; Duke, C. B. *Phys. Rev.* **1966**, *152*, 683–692.
- (14) von Roos, O. *Phys. Rev. B* **1983**, *27*, 7547–7552.
- (15) Franceschetti, A.; Zunger, A. *Phys. Rev. Lett.* **1997**, *78*, 915–918.
- (16) Bastard, G. *Phys. Rev. B* **1981**, *24*, 5693–5697.
- (17) Moiseyev, N.; Lefebvre, R. *Phys. Rev. A* **2001**, *64*, 052711:1–6.
- (18) This result can be derived based on the description given in ref 11.
- (19) Tuv, I.; Band, Y. B. *J. Chem. Phys.* **1997**, *107*, 9079–9084.
- (20) Fonseca, L. R. C.; Jimenez, J. L.; Leburton, J. P.; Martin, R. M. *Phys. Rev. B* **1998**, *57*, 4017–4026.
- (21) Laux, S. E.; Stern, F. *J. Appl. Phys.* **1986**, *49*, 91–93.
- (22) Jackson, J. D. *Classical Electrodynamics*; John Wiley & Sons, Inc.: New York, 1963.
- (23) Nicholson, D. M. C.; Shelton, W. A. *J. Phys.: Condens. Matter* **2002**, *14*, S601–S608.
- (24) Davidson, E. R. *J. Comput. Phys.* **1975**, *17*, 87–94.
- (25) Zhu, H.; Song, N.; Lian, T. *J. Am. Chem. Soc.* **2010**, *132*, 15038–15045.
- (26) Piryatinski, A.; Ivanov, S. A.; Tretiak, S.; Klimov, V. I. *Nano Lett.* **2006**, *7*, 108–115.